

PAPER • OPEN ACCESS

Enhanced ionisation of polyatomic molecules in intense laser pulses is due to energy upshift and field coupling of multiple orbitals

To cite this article: Sonia Erattupuzha *et al* 2017 *J. Phys. B: At. Mol. Opt. Phys.* **50** 125601

View the [article online](#) for updates and enhancements.

You may also like


- [Looking inside the tunnelling barrier: I. Strong field ionisation from orbitals with high angular momentum in circularly polarised fields](#)
Jivesh Kaushal and Olga Smirnova
- [Novel inferences of ionisation and recombination for particle/power balance during detached discharges using deuterium Balmer line spectroscopy](#)
K Verhaegh, B Lipschultz, B P Duval *et al.*
- [Electron and ion spectroscopy of camphor doped helium nanodroplets in the extreme UV and soft x-ray regime](#)
Sanket Sen, S Mandal, S De *et al.*



Easy-to-use and Helium-3 free
cryogenics solutions

LEARN MORE

Enhanced ionisation of polyatomic molecules in intense laser pulses is due to energy upshift and field coupling of multiple orbitals

Sonia Erattupuzha¹, Cody L Covington², Arthur Russakoff², Erik Lötstedt³, Seyedreza Larimian¹, Václav Hanus¹, Sergiy Bubín⁴, Markus Koch⁵ , Stefanie Gräfe⁶, Andrius Baltuška¹, Xinhua Xie (谢新华)¹, Kaoru Yamanouchi³, Kálmán Varga² and Markus Kitzler^{1,7}

¹ Photonics Institute, Technische Universität Wien, Gusshausstrasse 27, A-1040 Vienna, Austria

² Department of Physics and Astronomy, Vanderbilt University, Nashville, TN 37235, United States of America

³ Department of Chemistry, School of Science, The University of Tokyo, 7-3-1 Hongo, Bunkyo-ku, Tokyo 113-0033, Japan

⁴ Department of Physics, School of Science and Technology, Nazarbayev University, Astana, 010000, Kazakhstan

⁵ Institute of Experimental Physics, Graz University of Technology, Petersgasse 16, A-8010 Graz, Austria

⁶ Institute for Physical Chemistry, Friedrich-Schiller-University Jena, Helmholtzweg 4, D-07743 Jena, Germany

E-mail: lotstedt@chem.s.u-tokyo.ac.jp and markus.kitzler@tuwien.ac.at

Received 7 March 2017, revised 21 April 2017

Accepted for publication 2 May 2017

Published 31 May 2017



Abstract

We present the results of a combined experimental and numerical study on strong-field ionisation of acetylene performed with the aim of identifying the mechanism behind the previously reported surprisingly large multi-electron ionisation probabilities of polyatomic molecules. Using coincidence momentum imaging techniques and time-dependent density functional simulations, we show that the reported efficient ionisation is due to the combined action of a significant geometrically induced energy upshift of the most relevant valence orbitals as the C–H distance stretches beyond about two times the equilibrium distance, and a strong increase in the coupling between multiple molecular orbitals concomitant with this stretch motion. The identified enhanced ionisation mechanism, which we refer to as EIC-MOUSE, is only effective for molecules aligned close to parallel to the laser polarisation direction, and is inhibited for perpendicularly aligned molecules because of a suppression of the C–H stretch motion during the onset of ionisation.

Keywords: coupling of multiple orbitals, multiple ionisation and fragmentation of polyatomic molecules, enhanced ionisation

(Some figures may appear in colour only in the online journal)

⁷ Author to whom any correspondence should be addressed.

1. Introduction

When an atom or molecule is exposed to an intense laser field, the dominant process taking place is ionisation, i.e., the removal of one or several electrons by the action of the strong laser field. Strong-field ionisation is the prerequisite for

essentially all processes exploited for measurements in the sub-laser-cycle temporal domain and the production of attosecond pulses [1]. Strong-field ionisation of atoms is now reasonably well understood [2]. However, for molecules this process is still under intense investigation, since it is much more complex. In contrast to atoms, laser-ionisation of molecules is complicated by their structure and its dynamical changes that are initiated by the action of the laser field and that may subsequently take place during the laser pulse. An important discovery in the ionisation behaviour of molecules is that for diatomics the ionisation rate shows a strong variation with the internuclear distance, R . This phenomenon, known as enhanced ionisation (EI), has been investigated in numerous experimental and theoretical works for different molecular species, e.g., H_2/D_2 [3–11], I_2 [12–15], N_2 [16–18], and Cl_2 [19]. It was found that in many cases the ionisation rate is strongly enhanced around a critical internuclear distance, R_c .

This enhancement can be explained by a mechanism where at R_c electrons can tunnel directly into the continuum through the field-suppressed intra-molecular potential barrier from the potential well that is uplifted in energy by the laser field, when at the same time the electronic density localises on the upper potential well. This charge localisation on the upper potential well is due to a strong coupling between charge-resonance states, which is why this mechanism has been dubbed charge-resonance EI (CREI) [3, 4, 17]. Although this simple picture needs to be modified for certain situations such as for π or δ molecular states [8] or for non-symmetric molecules [20, 21], and in detail is affected by laser-sub-cycle electron dynamics [10, 11], CREI was found to be a general phenomenon and has been made responsible also for the EI observed in triatomic molecules such as H_3^+ [5, 9], NO_2 [22], N_2O [23] and CO_2 [24, 25], and for small [20, 21, 26, 27] and large van der Waals clusters [28]. While, overall, the underlying mechanisms leading to efficient single- or few-electron laser-ionisation in small molecules seem to be reasonably understood now and can in many cases be explained by (variants of) the CREI mechanism, the ionisation behaviour of larger polyatomic molecules containing three or more bonds, in particular for multi-electron ionisation, is still widely unexplored territory and a number of fundamental questions are yet to be answered.

Results of recent [29–32] and earlier [18, 19, 33] experiments on strong-field multiple ionisation of polyatomic molecules such as CH_4 , C_2H_2 , C_2H_4 , and C_4H_6 have been interpreted in terms of the existence of some enhancement mechanism for the ionisation. Very recent measurements on C_2H_2 were interpreted such that this enhancement is due to the CREI mechanism [32]. However, the results of recent theoretical works [30, 34, 35] are in contradiction to this interpretation and we will show below that the observed EI is indeed due to a different mechanism. In [29, 31] a multiple-bond version of EI, in which EI takes place at several bonds in parallel, was suggested to explain the surprisingly high charge states observed in these experiments. However, the underlying electronic mechanisms for this type of EI that can

explain the experimentally observed emission of up to 14 electrons [29] are still under debate.

Theoretical works using time-dependent Hartree–Fock (TDHF) to investigate EI of C_2H_2 [34, 36, 37] and time-dependent density functional theory (TDDFT) applied to CH_4 and C_4H_6 [30] as well as C_2H_2 and C_2H_4 [35] have confirmed the high charge states measured in these experiments as well as the experimentally found crucial role of concerted stretched multiple C–H bonds in the ionisation mechanism. As for C_2H_2 and C_2H_4 ionisation to charge states higher than four necessarily means the involvement of lower valence levels in the ionisation dynamics, a central question is how the laser field can efficiently remove electrons from them. The simulations on C_2H_2 [34, 35] have revealed an interesting mechanism, namely that the lower valence energy levels experience a significant field-free energy-upshift at stretched C–H bond configurations. This has two consequences: first, the reduced binding potential of the lower valence levels leads to an increase of the ionisation rate from these levels. Second, as the levels shift up, their energy spacing also decreases, which results in a stronger laser-driven coupling of the lower levels to higher energy states and therewith in increased ionisation from the lower states. Both effects result in a strong involvement of the lower valence orbitals in the ionisation process.

Following from this, a crucial parameter in the ionisation of C_2H_2 to high charge states should be the alignment of the molecular axis with respect to the laser polarisation direction. This is because both abovementioned contributions, ionisation from inner-valence orbitals and the coupling to higher states, strongly depend on the molecular alignment. This can be easily seen by the following considerations. For C_2H_2 the two most loosely bound orbitals feature π geometry, whose electron density peaks perpendicular to the molecular axis, while the more strongly bound orbitals feature σ geometry with a maximum of the electron density along the molecular axis. See figure 1(a) for a visualisation of the orbitals. As the contributions from the σ orbitals are crucial to reach higher charge states, based on these geometrical considerations one should expect a strong dependence of the ionisation rate on the molecular alignment [38–42]. Laser-induced coupling of inner orbitals with more loosely bound and also with initially unoccupied orbitals, on the other hand, is expected to show a similar or even stronger dependence on the alignment of the molecular axis with the laser polarisation direction. This is because the dipole transition matrix elements that determine these couplings are dictated by the geometrical overlap and symmetry of the different orbitals and their projections onto the laser polarisation direction. This point is somewhat reminiscent to the single-electron CREI process, which features an extraordinarily strong maximum of the coupling for parallel alignment due to the necessary charge-localisation [3–5, 14, 15]. However, the multi-electron, multi-orbital situation in C_2H_2 makes the ionisation process to charge states $\geq +4$ a much more complicated problem. Understanding the angular-dependence of the multi-electron ionisation process of C_2H_2 is thus of crucial importance for obtaining a better understanding of the EI process in polyatomic molecules in general [29].

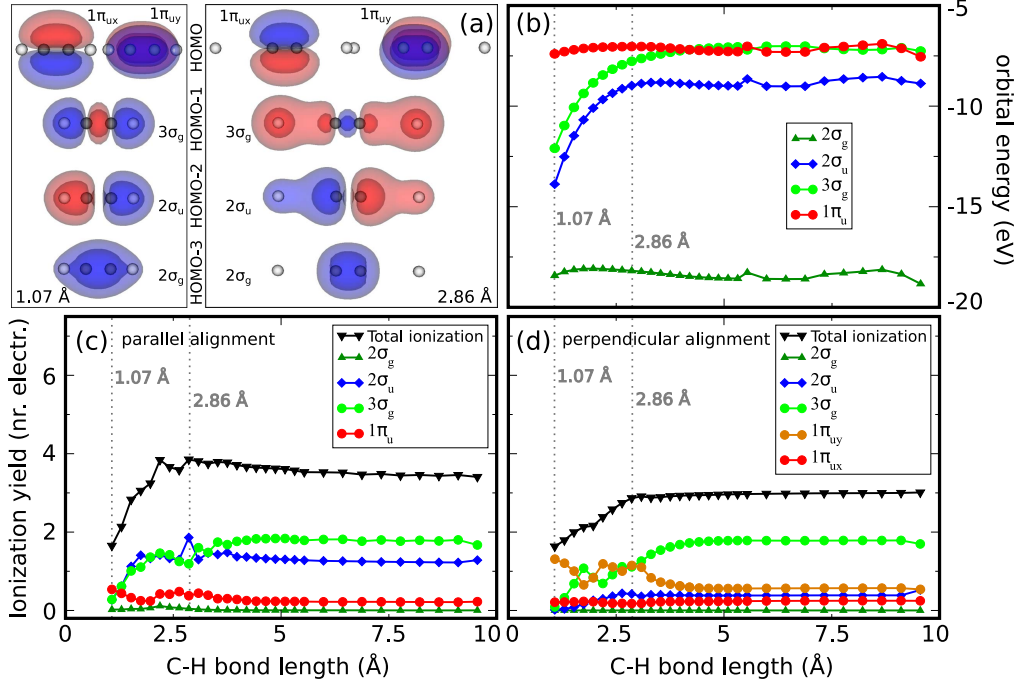


Figure 1. (a) Visualization of the five most weakly bound occupied Kohn–Sham orbitals, $\psi_k(\vec{r}, 0)$, of C₂H₂ in its equilibrium configuration at a C–H distance of 1.07 Å (left) and for symmetrically stretched C–H bonds at an internuclear distance of 2.86 Å (right). (b) Field-free binding energy of these valence orbitals as a function of the C–H internuclear distance (symmetric stretch mode) calculated by DFT. (c) Ionization yields in number of electrons lost from these orbitals as given by equation (6) for C₂H₂ molecules aligned parallel to the laser polarisation direction, simulated using TDDFT as a function of the C–H internuclear distance (assumed fixed in the simulations) for a laser pulse with a duration of 4.5 fs (FWHM of intensity) and a peak intensity of 7×10^{14} W cm^{−2}. See text for details of the simulations. (d) Same as (c) but for perpendicularly aligned molecules. The dashed vertical lines mark the C–H bond lengths 1.07 Å (equilibrium distance) and 2.86 Å used in figures 5 and 6 below.

Here we present the results of a combined experimental and theoretical study on strong-field ionisation of C₂H₂ performed with the aim of understanding the mechanism behind the crucial involvement of the lower lying valence orbitals in the efficient multi-electron ionisation process. To this end we performed four-body coincidence measurements of protons and multiply charged carbon ions created during the Coulomb explosion of C₂H₂ from charge states $z = +4$ up to $z = +9$ for a wide range of laser pulse durations and peak intensities. In order to obtain insight into the ionisation from lower valence levels and its dependence on the C–H distance we analyse the three-dimensional (3D) momentum distributions of the protons for different charge states. The experiments reveal a strong enhancement of the ionisation probability to charge states $z \gtrsim +4$ for molecules aligned parallel to the laser polarisation direction when the C–H internuclear distance stretches beyond roughly 2–2.5 times the internuclear distance, and a strong suppression of the ionisation probability for molecules aligned perpendicularly.

Our experiments together with the complementary insight obtained through quantum chemical simulations based on the TDDFT reveal that the strong ionisation enhancement for molecules aligned parallel is due to the combined action of (i) a significant geometrically induced energy upshift of the most relevant valence orbitals as the C–H distance increases, and (ii) a concomitant strong increase in the coupling between multiple molecular orbitals. Both processes lead to a strong effective

reduction of the binding energy and an enhancement of the emission probability from lower-valence orbitals, making their ionisation contributions even the dominant ones. For molecules aligned perpendicularly to the laser polarisation direction this mechanism is inhibited because of a dominant emission of π electrons at low charge states, which in turn suppresses the C–H stretch motion and therewith prohibits entering the regime of the EI. To express the two mentioned key-ingredients in this identified mechanism we would like to refer to it as EIC-MOUSE (Enhanced Ionisation from laser-Coupled Multiple Orbitals that are Up-Shifted in Energy). We argue that the EIC-MOUSE mechanism, which—as we will show—is different from CREI in many ways, can explain the high charge states measured for different hydrocarbons, e.g., [18, 29–33], and might also be at work in the multiple ionisation of other polyatomic molecules such as CO₂ [25].

2. TDDFT predictions of C₂H₂ ionisation

We start our analysis of the angular dependence of C₂H₂ multi-electron ionisation by discussing numerical predictions of TDDFT for the ionisation yields and binding energies for a fixed nuclear geometry as a function of C–H distance, shown in figures 1(b)–(d). Details about the numerical methods applied in the TDDFT simulations can be found in [30, 35]. In short, TDDFT is implemented on a real-space grid with

real-time propagation. Core electrons, which are difficult to handle computationally, were represented using norm-conserving Troullier–Martins pseudopotentials [43]. In the current simulations we considered 5 valence orbitals. Thus, 10 electrons were propagated and the remaining 4 electrons were kept frozen. The maximum number of electrons that could be emitted through ionisation was therefore 10.

The electronic ground state of C_2H_2 , from which we obtain the field-free energy for a fixed C–H distance, is computed by performing the ground-state DFT calculation and subsequently the time-dependent Kohn–Sham orbitals, ψ_k , are determined by solving the time-dependent Kohn–Sham equation

$$i\frac{\partial\psi_k(\vec{r}, t)}{\partial t} = H\psi_k(\vec{r}, t), \quad (1)$$

where k is a quantum number labelling the orbital. Here and throughout the paper we use atomic units (unless stated otherwise). The (Kohn–Sham) Hamiltonian is given by

$$H = -\frac{1}{2}\nabla_{\vec{r}}^2 + V_{\text{H}}[\rho](\vec{r}, t) + V_{\text{XC}}[\rho](\vec{r}, t) + V_{\text{ext}}(\vec{r}, t). \quad (2)$$

Here ρ denotes the electron (number) density, which is defined by the sum over all occupied orbitals

$$\rho(\vec{r}, t) = 2 \sum_{k=1}^5 |\psi_k(\vec{r}, t)|^2, \quad (3)$$

where the factor 2 takes into account that the Kohn–Sham orbitals ψ_k are always doubly occupied in the current simulations. V_{H} in equation (2) is the Hartree potential, defined by

$$V_{\text{H}}(\vec{r}, t) = \int d\vec{r}' \frac{\rho(\vec{r}', t)}{|\vec{r} - \vec{r}'|}, \quad (4)$$

and accounts for the electrostatic Coulomb interactions between electrons. V_{XC} is the exchange–correlation potential, whose exact form is a complicated functional of the entire history of the electron density. It is approximated using the adiabatic local-density approximation with the parametrization of Perdew and Zunger [44]. The last term in equation (2), V_{ext} , is the external potential, which includes the time-independent potential due to the ions, V_{ion} , and the explicitly time-dependent potential due to the electric field of the laser treated in dipole approximation $V_{\text{laser}} = \vec{r} \cdot \vec{E}(t)$ with $\vec{E}(t)$ the laser electric field. V_{ion} is a sum of norm-conserving pseudopotentials by Troullier and Martins [43] centred at each ion. The time-dependent orbitals, from which the electron density is calculated, are time-propagated from the initial state to some time, t , by using a fourth-order Taylor expansion of the time-evolution operator.

The ionisation behaviour predicted by the TDDFT simulations for C_2H_2 molecules aligned parallel and perpendicular to the laser polarisation direction, respectively, for different symmetric C–H distances is shown in figures 1(c) and (d). The laser pulse duration and peak intensity assumed in these and all other simulations in this work were 4.5 fs FWHM (full width at half maximum in intensity) and $7 \times 10^{14} \text{ W cm}^{-2}$, respectively, and the pulse shape and centre wavelength were Gaussian

and 790 nm, respectively, throughout. The ionisation yield is calculated from the Kohn–Sham orbitals $\psi_k(\vec{r}, t)$ as follows. The total number of electrons occupying a Kohn–Sham orbital k is defined as

$$n_k = 2 \int_V |\psi_k(\vec{r}, t)|^2 d\vec{r}, \quad (5)$$

where V is the total simulation volume. The simulation volume V is a cubic box with a side length of 34.25 Å and a volume of $V = (34.25 \text{ Å})^3$. A complex absorbing potential starting 5 Å from the edges of the box to absorb any outgoing probability density is used. The total ionisation yield (or the number of lost electrons) of each orbital after the laser-molecule interaction is

$$Y_k = 2 - n_k(T), \quad (6)$$

where T is a time large enough such that $n_k(t)$ is stationary. Y_k is what is shown in figures 1(c) and (d). The total ionisation yield is then given by

$$Y_{\text{tot}} = \sum_{k=1}^5 Y_k. \quad (7)$$

Throughout this work all simulations were performed with the C–H and C–C distances being kept fixed during time-propagation. The main motivation for working within the adiabatic Born–Oppenheimer (BO)-approximation with fixed nuclei, i.e., the approximation that the electron dynamics can be treated separately from the nuclear motion, is that it greatly increases the clarity of the analysis of the numerical data. Identification of EI for moving nuclei is a difficult and very likely also ambiguous task. For example, any analysis based on the symmetry of orbitals becomes impractical for moving nuclei. Thus, although we could previously identify the effect of the C–H stretch motion on the ionisation dynamics of acetylene during laser pulses as short as ≈ 5 fs [31], we consider the BO-approximation justified for the analysis performed below. This is because here our main interest lies on identifying the influence of electron excitation and orbital mixing for different molecular geometries, and these processes take place on very fast time-scales comparable to the laser-oscillations.

To include nuclear motion in the simulations explicitly, one could apply Ehrenfest dynamics as was done in [30, 35]. Within that scheme the motion of the nuclei is propagated from a set of initial positions and velocities concomitantly with the motion of the electrons. On the one hand this may increase the numerical effort considerably, depending on the number of propagated Ehrenfest trajectories. On the other hand, and more important for the questions considered here is, however, that this greatly complicates the analysis. The identification of the electron dynamics underlying the experimental results that we discuss below has been largely facilitated by our choice of fixed nuclei. Nevertheless, it would be desirable to complement our simulations with moving-nuclei simulations (of classical or quantum type). But given the numerical effort and complexity of the analysis this is beyond the scope of the current work.

In the processes considered in our work many electrons are simultaneously moving within the acetylene molecule. But this does not mean that electron–electron correlation is

important, as many-electron effects (e.g., multiple ionisation) should not to be equated with electron-correlation effects. In fact, electron–electron correlation in strong-field physics is a small effect if recollision-ionisation is not important [45, 46]. Still, through the exchange-correlation (XC) potential TDDFT actually does include electron correlation to some extent, although this potential is an approximation. In the cases considered in our work the interaction with the laser field is, however, much stronger than the XC functional or, even more so, the error in the XC functional. Good agreement between TDDFT ionisation rates and experimental results has been reported for example in [47, 48]. This demonstrates that TDDFT is capable of capturing the overall picture of several strongly driven electrons moving simultaneously in the laser field. For practical reasons, TDDFT is currently about the best one can do to model ionisation of polyatomic many-electron molecules. Methods including electron–electron correlation in a more accurate way are simply not available, or are much too expensive computationally.

The total ionisation yield calculated for different molecular geometries for both the parallel and perpendicular molecular alignment shown in figure 1 rises monotonically as the C–H bonds are symmetrically stretched from their equilibrium distance, and reaches a plateau around a C–H distance of 3 Å, about 3 times the equilibrium C–H distance. The absence of a clear critical internuclear distance at which the ionisation yield is enhanced as compared to shorter or longer C–H distances and the monotonic rise and saturation at large C–H distances is in agreement with the 3D TDHF simulations of [34]. The present TDDFT simulations predict that on average 4 electrons for parallel and about 3 electrons for perpendicular alignment of the molecule with the laser polarisation direction are emitted.

More interesting than the total ionisation yield is the ionisation yield from different molecular orbitals. It can be seen in figure 1 that for both parallel and perpendicular alignment at stretched C–H bonds it is predicted that the by far biggest share of the electron density is emitted from the lower-lying orbitals that feature initially σ -symmetry, rather than from the most weakly bound π -orbitals. In both cases most of the electron density originates from the $3\sigma_g$ orbital. For parallel alignment additionally the $2\sigma_u$ orbital contributes strongly, while contributions of this orbital are suppressed for perpendicular alignment. Instead, for perpendicular alignment at small C–H distances one of the most weakly bound $1\pi_u$ orbitals shows strong ionisation, but its contributions strongly decrease as the C–H bonds are stretched. This dominance of the $1\pi_u$ orbitals at small C–H distances for perpendicular alignment can be due to their shapes, which leads to maxima of the electron density perpendicular to the molecular axis [39].

Overall, TDDFT predicts that for stretched C–H bonds the dominant contributions come from the σ -orbitals. This behaviour can be partly understood by the aforementioned field-free energy upshift of the σ -orbitals with increasing C–H distance that has been predicted by previous simulations [34, 35] and that is also revealed in figure 1(b). It can be seen that at equilibrium geometry the σ -orbitals are quite strongly

bound, approximately 6 eV more strongly than the most weakly bound two degenerate π orbitals. As the C–H distance increases and the molecular geometry changes, however, the σ -orbitals become strongly upshifted in energy at field-free conditions, and around a C–H distance of 3–4 Å their binding energy becomes comparable to that of the π -orbitals. For still longer C–H distances >5 Å the $3\sigma_g$ orbital even becomes the most weakly bound orbital. Most notably, the range of C–H distances where the binding energy of the σ -orbitals strongly decreases coincides nicely with that where the ionisation yield strongly increases, compare to figures 1(c) and (d). Thus, the geometrically induced energy upshift very likely plays an essential role for the increase of the ionisation yield with increasing C–H distance and the dominant contribution of the σ orbitals. In addition, however, laser-induced coupling to higher lying states might be an important mechanism in the multi-electron ionisation dynamics of C_2H_2 .

3. Experimental results

3.1. Experimental approach and setup

To obtain further insight into the mechanisms underlying the multiple-ionisation of C_2H_2 we now turn to experiments. Experimentally accessible quantities that are sensitive to the degree of ionisation from lower-lying orbitals, to the C–H stretch motion, and potentially also to the coupling between lower- and higher-lying orbitals are 3D momentum distributions of protons that are generated during the Coulomb explosion of $C_2H_2^{z+}$ molecular ions into two carbon ions C^{m+}/C^{n+} and two protons, where $z = m + n + 2$. As for $z \geq +4$ the protons are ejected promptly after (and also already during) the interaction with the laser pulse and long before the carbon skeleton structure disintegrates [29–31], their momentum vector directly encodes the 3D-alignment of the molecule with respect to the laser polarisation axis at the time of the interaction, provided the interaction takes place quickly enough such that any rotational motion can be neglected during the time needed for the interaction and ejection processes [31, 49]. Owing to the light mass of the protons and the fact that their ejection takes place from high charge states this process is a very fast one [29–31], and we estimate that this is fulfilled in good approximation for the laser pulse durations used here ranging from 4.5 to 12 fs. The magnitudes of the proton momenta encode the C–H distance at the time of the prompt ejection, such that from the 3D proton momentum distributions the molecular geometry can be reconstructed. Finally, under these conditions, the proton momentum distributions are also a sensitive measure of the contributions of the lower-lying and outer orbitals to the overall ionisation signal based on the different shape of outer π and inner σ orbitals, as discussed above and previously also demonstrated experimentally [39, 40].

To measure the 3D proton momentum distributions for a certain charge state z we use coincidence momentum imaging based on the COLd Target Recoil Ion Momentum Spectroscopy (COLTRIMS) technique [50]. The experimental setup and data

reconstruction procedures have been described in detail previously [29, 31, 39, 51]. In short, the laser pulses, linearly polarised along the z -direction of the lab-frame coordinate system and propagating along the x -direction, interact in an ultra-high vacuum chamber (background pressure $\sim 10^{-10}$ mbar) with randomly aligned C_2H_2 molecules provided by a supersonic gas jet, created by expanding about 1 bar of acetylene gas (Linde) at room temperature through a nozzle with a diameter of $10\ \mu\text{m}$ into a vacuum chamber at $\sim 5 \times 10^{-5}$ mbar operating pressure. The gas jet propagates along the y -coordinate of the lab-frame coordinate system. The fragment ions resulting from the interaction of a single molecule with a single laser pulse are guided by a weak homogeneous electric field of about $40\ \text{V cm}^{-1}$, applied along the z -coordinate of the lab-frame system, over a length of 5.7 cm to a position and time sensitive detector, where the positions and flight times of the fragments are recorded in coincidence. From this information the 3D momentum, \vec{p} , of each detected fragment ion is calculated. By imposing four-body momentum conservation conditions in all three spatial direction of the lab-frame coordinate system we selected sets of four ions, two carbon ions C^{m+}/C^{n+} and two protons with $z = m + n + 2$, generated by Coulomb explosion of a single acetylene molecular ion with charge state z [51]. Thus, it is ensured that all measured data shown below correspond to a certain charge-state z , and that all dynamics leading to the Coulomb explosion takes place within a single molecular ion.

Few-cycle laser pulses are generated by spectral broadening of 25 fs laser pulses with a spectrum centred at 790 nm from a titanium-sapphire laser amplifier system in a 1 m long hollow-core glass capillary filled with neon at several atmospheres pressure. Temporal compression of the pulses after the capillary by several bounces from pairs of chirped mirrors and subsequently passing them through a pair of glass wedges for fine-tuning the dispersion results in a pulse duration of ~ 4.5 fs. The duration and intensity-stability of the pulses are monitored on a shot-to-shot basis by a stereo-ATI phase-metre [52, 53]. The pulses are directed into the ultra-high vacuum chamber, where they are focused onto a supersonic gas jet of acetylene molecules by a spherical mirror with a focusing length of 60 mm.

The pulse duration was varied outside the vacuum chamber by positively chirping the shortest pulses by propagating them through different amounts of fused silica (FS). We confirmed that the sign of chirp is not of crucial importance for the results presented below. For this we re-measured some of the data with negatively chirped pulses with pulse durations up to about 10 fs and obtained very similar 3D proton momentum distributions. The peak intensity of the pulses in the measurement chamber was adjusted by reflecting the beam off a thick FS block under different angles, thereby changing the pulse energy. Calibration of the peak intensity on target was done with an estimated precision of $\pm 15\%$ by separate measurements using single ionisation of He atoms in circularly polarised light [54, 55].

3.2. Proton momentum distributions

Figure 2 shows cuts through measured momentum distributions of protons in the p_y - p_z -plane with $|p_x| < 10$ au for

pulse durations 4.5 and 12 fs and different peak intensities ($2.4, 7$ and $15 \times 10^{14}\ \text{W cm}^{-2}$), for charge states z ranging from $+4$, the lowest charge state permitting complete fragmentation of an acetylene molecular ion into four charged particles, up to $z = +7$. Charge states up to $+9$ were detected in our experiments. The 3D proton momentum distributions are the results of four-body coincidence selections as described above. Because the two protons are ejected simultaneously in a back-to-back manner, due to momentum conservation the proton momentum distributions are identical (within experimental resolution) for both protons. Figure 2 depicts the momenta of that protons reaching the detector earlier and the momentum distributions were mirrored about the p_y -axis. The back-to-back ejection scenario was confirmed using two-proton coincidence and carbon energy distributions, see the [appendix](#). As a consequence of this ejection and the prompt Coulomb explosion dynamics discussed above, the proton momentum vectors reflect the instantaneous alignment of the randomly aligned molecules during the interaction with the short laser pulse. The yield of protons for a certain charge state z at a certain angle with respect to the laser polarisation direction therefore directly relates to the probability to ionise acetylene molecules to this charge state.

The proton momentum distributions in figure 2 contain a number of important features that permit obtaining insight into the ionisation and fragmentation process of acetylene molecules in intense laser pulses. The first noteworthy feature is that the emission of protons peaks towards the laser polarisation direction (vertical in figure 2) for all pulse durations and intensities (in fact for all measurements we performed). To follow the pulse parameter dependence of the momentum distributions we derived angular distributions of the proton yield by integrating them over the momentum magnitude. The resulting distributions are shown in figure 3. From them it becomes clear that the cone of proton emission gradually becomes narrower and more elongated along the laser polarisation direction with increasing charge state for 4.5 fs pulses (for the high peak intensity used for this pulse duration) but not for 12 fs pulses. This points to a qualitative change in the ionisation mechanism if the intensity is decreased and the pulse duration is increased from 4.5 to 12 fs.

The second noteworthy feature that becomes apparent from the number of counts in the momentum distributions for different charge states z in figure 2 is that, on the one hand, not surprisingly, pulses with higher peak intensity tend to produce higher charge states. However, on the other hand, and more relevant to EI, it can also be seen that a 12 fs pulse with lower intensity can produce higher charge states than a roughly twice as intense 4.5 fs pulse (compare the left with the right column in figure 2). This again highlights the qualitative difference between 4.5 and 12 fs pulses. This pulse parameter dependence has been studied exhaustively in [31] and is explained by the time that the C-H bonds need for stretching to a bond-length at which the ionisation (of especially electrons in inner-valence orbitals) becomes enhanced. TDDFT predicts that this distance is roughly $3\ \text{\AA}$, see figure 1. For very short pulses the probability that the C-H bonds

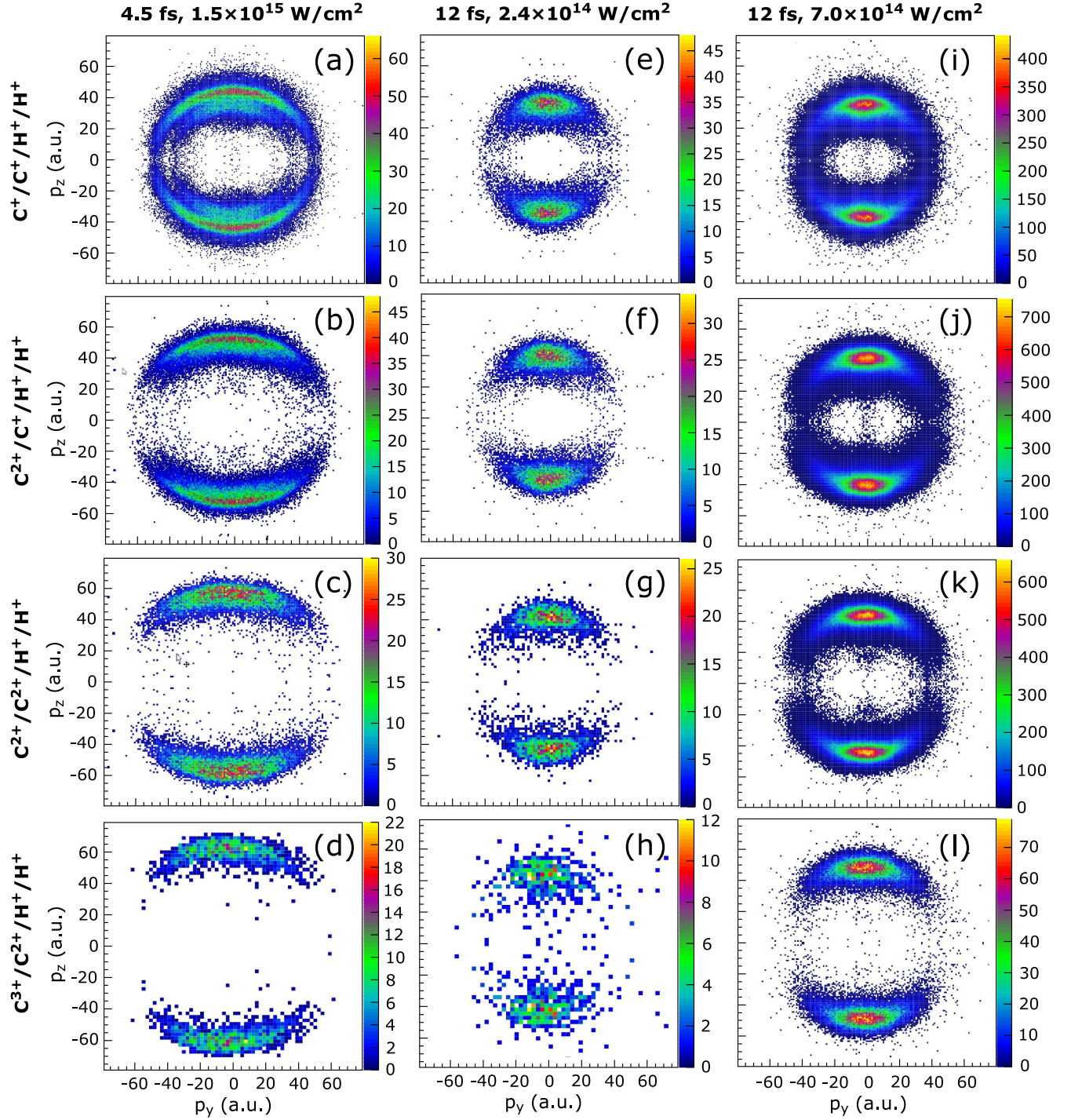


Figure 2. Measured momentum distributions of protons ejected during Coulomb explosion of C_2H_2^+ molecular ions into fragments $\text{C}^{m+}/\text{C}^{n+}/\text{H}^+/\text{H}^+$, with $z = m + n + 2$, in the p_z - p_y momentum plane with $|p_x| < 10$ au, resulting from a four-body coincidence selection. The laser polarisation direction is along p_z . Depicted is the momentum of that proton arriving at the detector first. The distributions have been symmetrized by mirroring them about the p_y axis. The laser pulse durations (FWHM) and peak intensities were (a)–(d) ~ 4.5 fs and $1.5 \times 10^{15} \text{ W cm}^{-2}$, (e)–(h) 12 fs and $2.4 \times 10^{14} \text{ W cm}^{-2}$, and (i)–(l) 12 fs and $7 \times 10^{14} \text{ W cm}^{-2}$. The rows are sorted by increasing charge state ranging from $z = +4$ (top row) to $z = +7$ (bottom row). The fragmentation channels are also indicated on the left.

stretch so far within the high-intensity window of the pulse is very small and therefore only a small percentage of molecules can reach the region of EI. For sufficiently long pulses this probability increases dramatically. It has been shown that pulses with a duration $\gtrsim 10$ fs fulfil this requirement related to the C–H stretch vibrational motion [31].

The transition to the regime of EI at stretched C–H bonds is reflected in the proton energy distributions as a function of intensity shown in figure 4 for 4.5 and 12 fs pulses for two different charge states (+4 and +6), depicted in the left and right columns, respectively. The proton energy distributions are derived from the momentum distributions by integrating

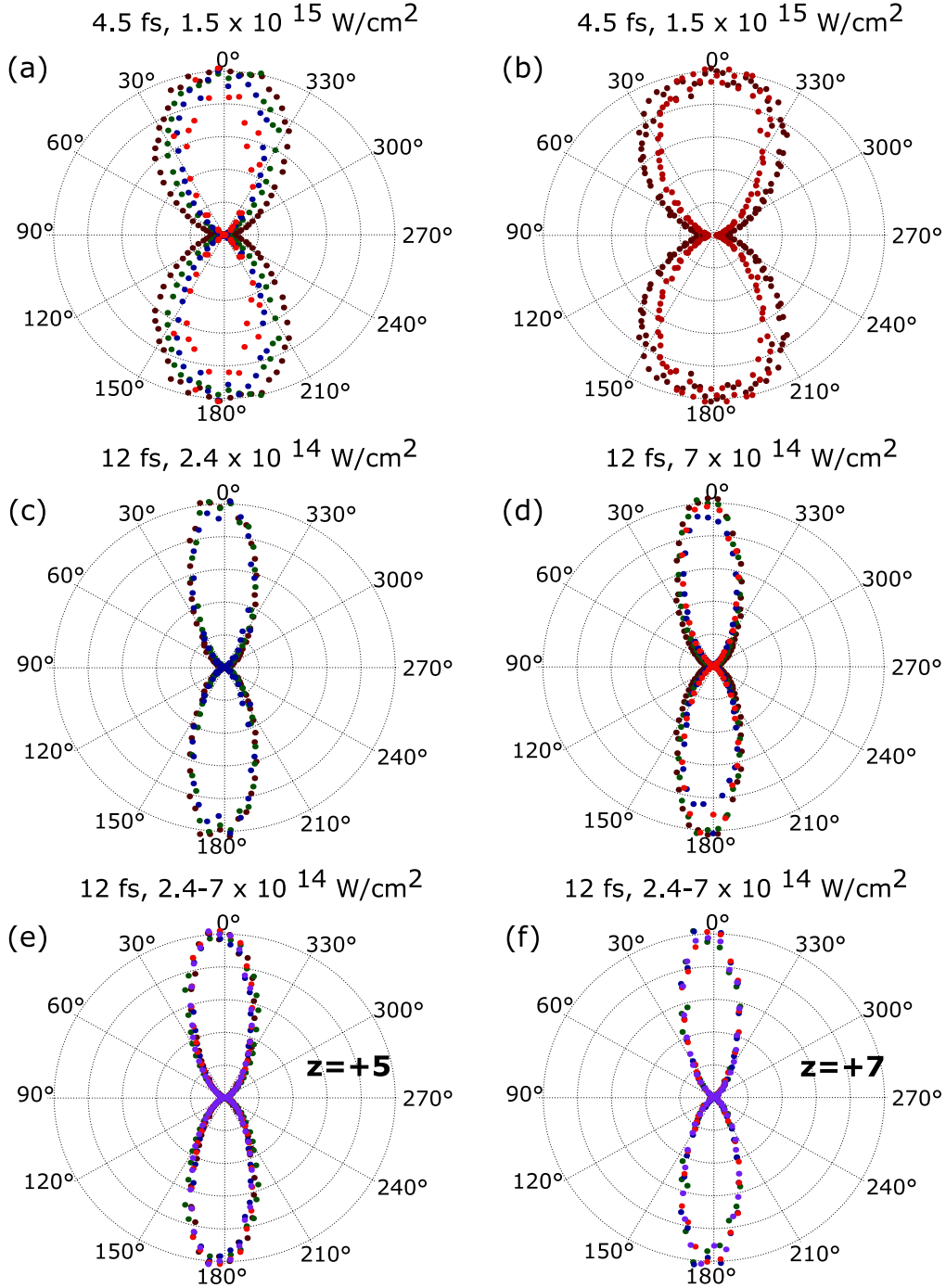


Figure 3. Polar plots of measured proton yields derived from figure 2 by integrating them in a polar coordinate system with coordinates $(|\vec{p}|, \theta)$ along the radial $|\vec{p}|$ direction. Depicted is the integral value $\Gamma(\theta)$ as a function of θ for different laser pulse parameters and four-body fragmentation channels $C^{m+}/C^{n+}/H^+/H^+$, $z = m + n + 2$, as indicated in the panels. $\theta = 0$ is along the direction of the laser polarisation (vertical). Panels (a), (c) and (d) depict $\Gamma(\theta)$ for different (m, n) with the colours brown, green, blue and orange indicating charge states $z = \{+4, +5, +6, +7\}$, respectively. The laser pulse durations (FWHM) and peak intensities were (a), (b) ~ 4.5 fs and $1.5 \times 10^{15} \text{ W cm}^{-2}$, (c) 12 fs and $2.4 \times 10^{14} \text{ W cm}^{-2}$, and (d) 12 fs and $7 \times 10^{14} \text{ W cm}^{-2}$. Panel (b) shows $\Gamma(\theta)$ for $m = n = 1$ for two different proton energy ranges (≤ 12 eV, lighter colour; > 12 eV, darker colour). Panels (e) and (f) depict $\Gamma(\theta)$ for $z = +5$ and $z = +7$, respectively, for pulse duration 12 fs and different laser peak intensities 2.4, 4.5, 5.7, 6.4 and 7 (in units of $10^{14} \text{ W cm}^{-2}$) indicated by the colours brown, green, blue, orange and purple, respectively.

over all ejection directions and using the correspondence $E_p = |\vec{p}|^2 / (2m_p)$ between proton momentum \vec{p} and energy E_p , where m_p denotes the proton mass. Figure 4 shows that the proton energy distributions measured for 4.5 fs pulses

with high laser intensity (for both depicted charge states) exhibit peaks at higher values of E_p than the proton distributions for 12 fs. The appearance of these high-energy peaks are an interesting, thus far not observed effect. They are

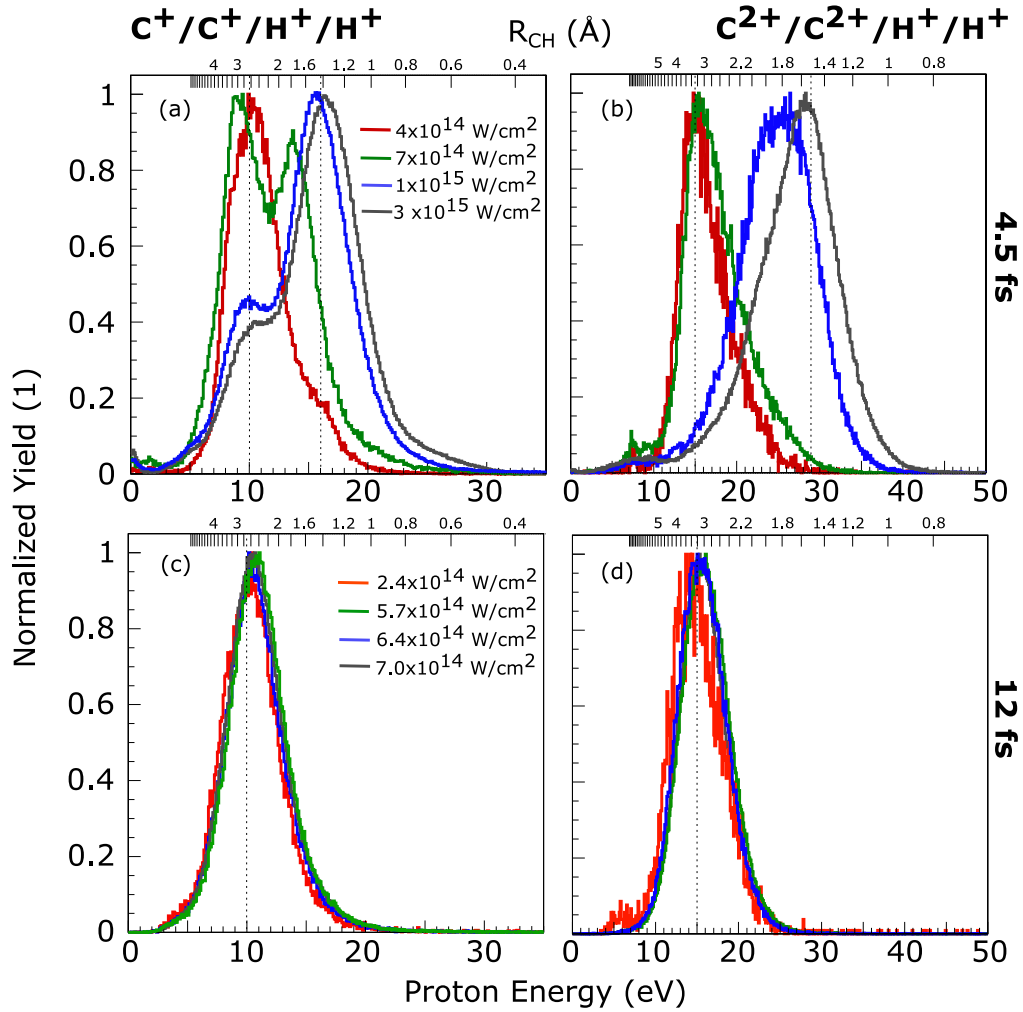


Figure 4. Measured proton energy distributions for different pulse peak intensities and durations, for two different four-body fragmentation channels $C^{m+}/C^{n+}/H^+/H^+$ with $m = n = 1$ (left) and $m = n = 2$ (right), as also indicated in the figure. The upper scale in each panel shows R_{CH} in Å calculated by equation (8). Energy values of peaks referred to in the text are indicated by vertical dashed lines. Pulse duration (FWHM) is 4.5 fs for (a), (b) and 12 fs for (c), (d). Laser peak intensity is assigned by colour as indicated in (a) for (a), (b) and (c) for (c), (d), respectively.

the third noteworthy feature in the proton momentum distributions. In figure 2 these features are visible as segments respectively peaks at high proton momenta. For $z = +4$ the high energy peak leads to a bimodal proton momentum distribution. For higher charge states only the peak at high momenta is visible in figures 2 and 4. With decreasing laser intensity the peak at high proton energy observed for 4.5 fs pulses gradually moves towards the lower values that are observed with the 12 fs pulses for all pulse peak intensities used in the experiments.

3.3. Proton energy distributions: role of C–H stretch motion

The proton energy can be related to the internuclear-distance at which the C–H bonds break during the proton ejection process [31]. Thus, the distributions in figure 4 allow for insight into the C–H stretch motion during the ionisation dynamics. For a certain charge state and intra-molecular charge distribution the C–H internuclear distance, R_{CH} , at the time of proton ejection can be calculated by assuming that

the protons gain energy purely by Coulomb repulsion from the remaining intra-molecular charges. By modelling the protons as point charges, located at a distance R_{CH} from their respective neighbouring carbon atoms in a linear molecular geometry, and by assuming that the remaining positive charge $z - 2$ is concentrated at the centre point between the two carbon ions, the C–H distance at the time of Coulomb explosion can be estimated from the proton energy, E_p , using equation (8)

$$E_p = \frac{z - 2}{R_{CH} + R_{CC}/2} + \frac{1}{4(R_{CH} + R_{CC}/2)}. \quad (8)$$

In deriving equation (8) we have tacitly made use of the fact that the ejection of protons happens much earlier and uninfluenced by the carbon ion dynamics justified in the appendix using the two-proton momentum and carbon energy distributions (figure A1). Another assumption is a symmetric distribution of the remaining positive charge $z - 2$ with respect to the molecular centre. The validity of this assumption is proven by the single-peaked smooth shape of the

carbon energy distributions in figure A1. We note that equation (8) can be further refined to spatially extended distributions of the positive charge $z - 2$ on the carbon skeleton structure, for example by assuming two positive point charges $(z - 2)/2$ at two arbitrary points in between the two carbon atoms rather than only a single point charge in the centre. Simulations show, however, that the proton energy becomes to a good approximation independent of the actual charge distribution in between the two carbon atoms for $R_{CH} \gtrsim 1.5$ Å. As a result, from the measured proton energy the C–H internuclear distance at which the proton ejection takes place can be retrieved using equation (8).

The decrease of the proton energy with pulse duration and intensity is thus a signature of the C–H stretch motion. By assuming $R_{CC} = 1.2$ Å, which is the equilibrium C–C internuclear distance of acetylene [56], we obtain from equation (8) for the high energy peaks in figure 4 at roughly 16 and 29 eV for $z = +4$ and $z = +6$, respectively, R_{CH} values of 1.4 and 1.5 Å. From the lower energy peaks at 10 eV ($z = +4$) and 15 eV ($z = +6$) we obtain R_{CH} values of 2.6 Å and 3.5 Å, respectively. For comparison, the equilibrium C–H distance $R_{CH}^{eq} = 1.07$ Å. This means, the lower proton energy peaks that are measured with 12 fs pulses for all intensities correspond to fragmentations from a geometry where the C–H bonds are significantly stretched. The transition to lower proton energies (see figure 4) as the pulses become weaker and longer, towards the minimal energy value that is observed with 12 fs pulses (for all measured intensities) is thus directly related to the C–H stretch motion during the ionisation. The reconstructed C–H distances for the low-energy peaks (2.6–3.5 Å) are in very good quantitative agreement with the bond lengths where the TDDFT simulations predict that the ionisation starts to saturate and the σ -orbitals reach their highest energy values, see figure 1. As the C–H bonds stretch and the ionisation from the inner-valence orbitals becomes enhanced also the angular distributions become significantly narrower, see figure 3. The dependence of this narrowing on the laser pulse parameters allows obtaining insight into the transition of the ionisation mechanism that takes place as the C–H bonds stretch, as will be discussed in the following section 3.4.

3.4. Transition in ionisation mechanism with pulse parameters

We start the discussion by exploring the origin of the peak at high proton momenta that is observed with intense 4.5 fs pulses (figures 2(a)–(d)). Figure A1 in the appendix visualises the transition from low to high proton momenta for charge states $z = +4$ as the laser peak intensity is increased. From those coincidence plots it becomes apparent that the energetic protons are also ejected back-to-back, just as the protons in the low energy peaks. This justifies application of equation (8), from which we find that these high-energy protons are ejected from significantly smaller C–H distances for all observed charge states. Thus, for short pulses and high laser peak intensities ionisation at shorter C–H distances close to the equilibrium distance becomes the dominant mechanism, in particular for ionisation to higher charge states. Obviously this means that for the very short pulses there is simply too little time for the C–H

bonds to stretch to $\gtrsim 2.6$ Å where ionisation from the lower lying orbitals becomes enhanced due to their geometrically induced energy upshift (figure 1) until the peak of the pulse where the ionisation rate reaches its maximum. This lack of time becomes more and more critical, the more electrons need to be removed before or at the peak of the laser pulse. Therefore, for high charge states $z \gtrsim +6$ exclusively the high-energy peak shows up, while for $z = +4$ small signatures from the contributions at stretched bonds are still visible. This type of ionisation at the short C–H distances thus dominantly builds on the high field-ionisation rate for high intensities rather than on the molecular mechanisms that we are after here, i.e., the beneficial contributions of the upshifted energy levels or coupling to higher energy levels. Naturally, this field-dominated mechanism is restricted to high pulse peak intensities. As the intensity is decreased, it is no longer possible to ionise the molecules to $z > +4$ at short C–H distances due to the high ionisation potential of the lower-valence levels, and ionisation at stretched bonds becomes the dominant mechanism, as can be seen clearly in figure 4 by the downshift of the proton energy for decreasing peak intensity.

The experiments thus clearly demonstrate that there is a qualitative transition in the ionisation mechanism between low and high laser peak intensities. For low peak intensities, high charge states are only reached if ionisation takes place at stretched bonds. This is true also for very short pulses around 5 fs, because the necessary stretch of the C–H bonds is small and this motion is very fast, albeit the probability to reach high charge states is strongly reduced as compared to longer pulses $\gtrsim 12$ fs. These findings confirm earlier ones [31].

How can this transition in the ionisation mechanism be seen in the angular ionisation probabilities plotted in figure 3? We have already noted above that the ionisation probability peaks along the laser polarisation direction for all charge states $z \geq +4$ and all pulse parameters. This is in agreement with the numerical results obtained by TDDFT shown in figure 1 and also with [35]. However, the ionisation probability is significantly more directional along the laser polarisation direction for 12 fs pulses than for the more intense 4.5 fs pulses (figure 3). Moreover, while for the 12 fs pulses a narrow angular distribution is observed for all charge states and intensities (in between 2.4×10^{14} and 7×10^{14} W cm⁻²), it is significantly broader and becomes gradually narrower and more elongated along the laser polarisation direction with increasing charge state for the intense 4.5 fs pulses. On a fine scale one can notice that also the distributions measured with the 12 fs pulses become slightly narrower with increasing charge states. But the dependence is much weaker than in the distributions measured with the 4.5 fs pulses. The qualitative change in the ionisation mechanism between the intense 4.5 fs and the weaker 12 fs pulses that is visible in the decrease of the proton energy is thus also clearly reflected in the angular distributions of the ionisation probability.

4. Discussion of the ionisation mechanism

Having established in section 3 the sensitivity of the proton angular yield distributions on the laser pulse parameters and

the transition in the ionisation mechanism between long and short, weaker and more intense pulses, we can now relate the angular dependence of the ionisation probability to the shape of the orbitals that are involved in the ionisation process. As we will see, this allows one to obtain an intricate insight into the multi-electron ionisation mechanism.

4.1. *EI regime at stretched bonds: strong ionisation contributions from lower-lying orbitals*

Because, as outlined above, the electron density of π -type orbitals shows a maximum perpendicular to the molecular axis while that of σ -type orbitals maximises along the molecular axis (figure 1), narrow angular distributions along the laser polarisation axis indicate a dominant contribution of ionisation from σ -orbitals, while broader angular distributions suggest that π -orbitals are involved in the ionisation process. The strong difference in the shape of the angular distributions between the intense 4.5 fs and the weaker 12 fs pulses (figure 3) can thus be related to a dominance of ionisation from σ -orbitals in the latter case, while their broader shape in the former case indicates a strong contribution from π -orbitals. This is understandable, as we showed above that the ionisation mechanism in the case of the longer pulses builds on stretched C–H bonds for which we, based on the TDDFT predictions in figure 1 and on earlier findings [34], should expect a strong enhancement of the ionisation from σ -orbitals, such that the ionisation yield is dominated by contributions from these orbitals. The very weak dependence of the narrow angular yield distributions on the charge state for the longer pulses might then be due to the fact that the geometrically induced energy upshift of the field-free inner-valence σ -orbitals levels off from a certain value of the C–H distance on and we should expect a plateau of EI rather than a clear critical internuclear distance, see figure 1 and [34]. Thus, for the multi-electron ionisation process that starts when the C–H bonds stretch into this plateau region, the angular yield distributions are expected to be dominated by ionisation from σ -orbitals throughout the process of (sequentially) removing many electrons (up to 9 in our measurements) and we should expect a narrow shape for all charge states, in agreement with our measurements (figure 3). Concomitant with the ionisation process the C–H bonds proceed their stretching motion within this plateau region, as is reflected by the increasing R_{CH} values that we reconstruct from our data using equation (8) [$R_{\text{CH}} = 2.6 \text{ \AA}$ for $z = +4$ and 3.5 \AA for $z = +6$]. The slight narrowing of the distributions with increasing charge state that can be noticed in figure 3 can then be attributed to the repeated removal of electrons from σ -type orbitals, which results in a repeated convolution of two narrow distributions and thus in decreasing width for higher charge states. The picture that emerges from all these observations thus confirms the predictions of both TDDFT (figure 1) and TDHF [34], namely that the ionisation is enhanced over an extended plateau region of C–H bond lengths rather than only at a critical distance.

Further confirmation for this picture, where ionisation is dominated by ionisation from lower-lying σ -type orbitals for

stretched C–H bonds and throughout their stretch motion, comes from the observation that the angular dependence of the ionisation yield does not depend on the laser intensity. Figure 3 shows that the yield of molecules ionised to high charge states (charge states $z = +5$ and $z = +7$ are depicted exemplarily) by 12 fs pulses exhibits the same narrow angular distribution for all measured intensities (2.4×10^{14} – $7 \times 10^{14} \text{ W cm}^{-2}$). This indicates that the ionisation takes place in the same manner within this intensity range, and the electrons are removed mainly from σ -type orbitals at stretched C–H bonds. Naturally, the total yield decreases with decreasing intensity, as is also reflected in the smaller count numbers for 2.4×10^{14} than for $7 \times 10^{14} \text{ W cm}^{-2}$ that can be seen in figure 2.

4.2. *Ionisation at small C–H distances: no assistance from lower-lying orbitals*

In contrast, if we now turn to the angular distributions of the ionisation yield measured with the intense 4.5 fs pulses shown in figure 3(a), we find that they are much broader than those measured with the weaker 12 fs pulses and that they vary significantly with charge state z , i.e., they become narrower with increasing z . The fact that they are much broader is in agreement with the finding that in this case the C–H bonds do not stretch much during the ionisation process, as described above. In this regime, according to figure 1 and [34], the binding energies of the σ -type orbitals are still significantly higher than those of the π -type orbitals and we can expect a dominating contribution from the latter orbitals to the overall electron yield. Indeed, the TDDFT simulations predict that at small C–H bond lengths the dominant contributions to the overall yield come from the π -orbitals and that the ionisation probability is only weakly higher for molecules aligned parallel than perpendicular to the laser polarisation direction (figure 1). Our experimental observation of a relatively broad angular distribution, shown in figure 3(a), is therefore in line with strong ionisation contributions from the outer π -type orbitals.

It needs to be noted, though, that the simulated results in figure 1 show the overall ionisation probability integrated over all charge states, including $z = +1, +2, +3$, which are not considered in the experimental data. It is inherently impossible to disentangle in the simulations the contributions from different orbitals to a certain charge state. Because, naturally, lower charge states z are produced with higher probability than those with $z \geq +4$, the overall ionisation probability integrated over all charge states is smaller and the simulations predict that *on average* only four electrons are removed during the ionisation process. That does not mean, however, that higher charge states are in disagreement with the TDDFT simulations. In fact, a mean value of $z = +4$ means that significantly higher charge states *must* contribute to the average. In the experiments we can, in contrast to the simulations, extract momenta for a certain charge state based on the four-body coincidence selection described above. A direct quantitative comparison of the experimental angular distributions in figure 3 for a certain charge state with the

simulated ionisation probability for parallel and perpendicular molecular alignment in figure 1 is thus not possible. The simulated high ionisation yield for perpendicular alignment that suggests a very uniform angular distribution of the ionisation yield should thus be narrower if only charge states $z \geq +4$ could be selected, since the lower charge states are dominantly produced by ionisation from the π -orbitals [41, 42]. With this in mind, the simulations confirm our interpretation that the broader shape of the experimentally observed angular distributions is due to strong ionisation contributions from π -orbitals.

With increasing charge state the measured angular distributions become significantly narrower (figure 3(a)). This can be seen as a signature of increasing contributions from σ -type orbitals. Clearly, for higher charge states these contributions must necessarily become stronger since the π -type orbitals can contribute with at most four electrons to the ionisation yield. But also the C–H bonds do undergo some small stretch motion as the ionisation proceeds as we have shown above. However, the stretch motion is clearly much smaller in the case of 4.5 fs pulses than for 12 fs pulses (we have estimated above roughly only half the values for R_{CH}). Therefore the molecules never completely reach the plateau of C–H bond lengths where the ionisation becomes enhanced, but there will be at least some increase of the ionisation probability from σ -type orbitals as the ionisation proceeds, which results in the narrower angular distributions for higher charge states that we observe in our experiment.

This explanation can be corroborated using the two peaks in the momentum distributions for $z = +4$ shown in figure 2(a). In our analysis in section 3, with the help of R_{CH} values obtained from equation (8), we have attributed the peak at lower proton momenta to ionisation at stretched C–H bonds, whereas the peak at high momenta is due to ionisation at short C–H bonds. Because the peak at lower proton momenta is due to ionisation and subsequent fragmentation when the C–H bonds stretch to the region where the binding energy of the σ -type orbitals is decreased, we expect for this peak a higher contribution to the four removed electrons from the σ -type orbitals than for the peak at higher proton momenta; the angular yield distribution should thus be narrower for the lower-energy peak than the high-energy peak. Indeed this is the case, as shown in figure 3(b) which plots the angular distributions of the two peaks separately based on a distinction in proton energy (using 12 eV as the border), thus visualising the higher ionisation contribution from the σ -type orbitals to the low-energy peak (data points with lighter colour in figure 3(b)). The angular distribution is not as narrow, though, as the one in the corresponding peaks at low proton momentum/energy measured with 12 fs pulses. This can partly be due to the contributions from the lower energy tail of the high energy peak that are still present in the angular distributions when separating the two peaks in energy, see shape of the proton energy distributions in figure 4(a).

4.3. Role of field-induced coupling with and population transfer to loosely bound orbitals

By analysis of the measured proton momentum distributions for different laser pulse parameters we could show that the C–H stretch motion and the energy upshift of the field-free inner-valence σ -type orbitals accompanying this stretch motion that has been predicted theoretically—see [34, 35] and figure 1—are key ingredients in this multi-electron process that has been observed for a number of different hydrocarbons [29] and that has since then been the subject of a number of investigations, e.g., [30, 31, 34–37]. However, this simple interpretation based purely on the shape of the angular yield distributions in comparison to the shapes of the orbitals' electron density neglects an important process, namely laser-induced coupling between the different orbitals, which in simulations was found to be another important ingredient in the ionisation mechanism [34, 36, 37]. The potential importance of laser-induced couplings and electron probability transfer to higher levels seems very reasonable considering that when the energy levels come close, the coupling between them by the laser electric field is also expected to strongly increase. The strong coupling between the HOMO and the LUMO at large internuclear distances is essential for the CREI mechanism described for the H_2^+ molecule [4]. And it has also been shown by TDHF simulations [34, 36, 37] that the coupling between different bound levels is expected to be an essential feature in the ionisation behaviour of C_2H_2 . The influence of this process on the multi-electron ionisation dynamics we will discuss in the following using numerical results obtained by TDDFT simulations.

In order to investigate the role of laser-driven couplings between different orbitals—in particular to initially unoccupied ones—in the multi-electron ionisation process we calculated the evolution during the laser pulse of the projections of the time-propagated Kohn–Sham orbitals, $\psi_i(\vec{r}, t)$, onto the ground state orbitals $\psi_j(\vec{r}, t = 0)$, i.e., $\langle \psi_i(\vec{r}, t) | \psi_j(\vec{r}, 0) \rangle$. The absolute values squared of these quantities, $P_{ij}(t) = |\langle \psi_i(\vec{r}, t) | \psi_j(\vec{r}, 0) \rangle|^2$, measure the probabilities $P_{ij}(t)$ how much during the laser-interaction a certain orbital $\psi_i(\vec{r}, t)$ gets depopulated, and how much of this depopulation is due to coupling to other orbitals. Depopulation of an orbital is measured by the decrease of the quantity $P_{ii}(t)$ from its initial value 1, coupling to other orbitals is measured by the quantities $P_{ij}(t)$. From figure 1 we know that the two orbitals that contribute the most to the overall ionisation yield are $3\sigma_g$ (HOMO-1) and $2\sigma_u$ (HOMO-2). Therefore, in the following analysis we will focus on these two orbitals, although in our simulations we have also access to the projections of the other time-dependent orbitals.

The quantities $P_{3\sigma_g,j}(t)$ and $P_{2\sigma_u,j}(t)$ for selected orbitals $\psi_j(\vec{r}, 0)$ are plotted in figure 5 for the two cases where the molecular axis is aligned parallel and perpendicular to the laser polarisation direction, respectively. For the parallel alignment we show the data for a C–H distance 2.86 Å where the total ionisation yield starts to saturate (see figure 1), for perpendicular alignment we show it additionally for the equilibrium C–H distance 1.07 Å. The laser parameters are

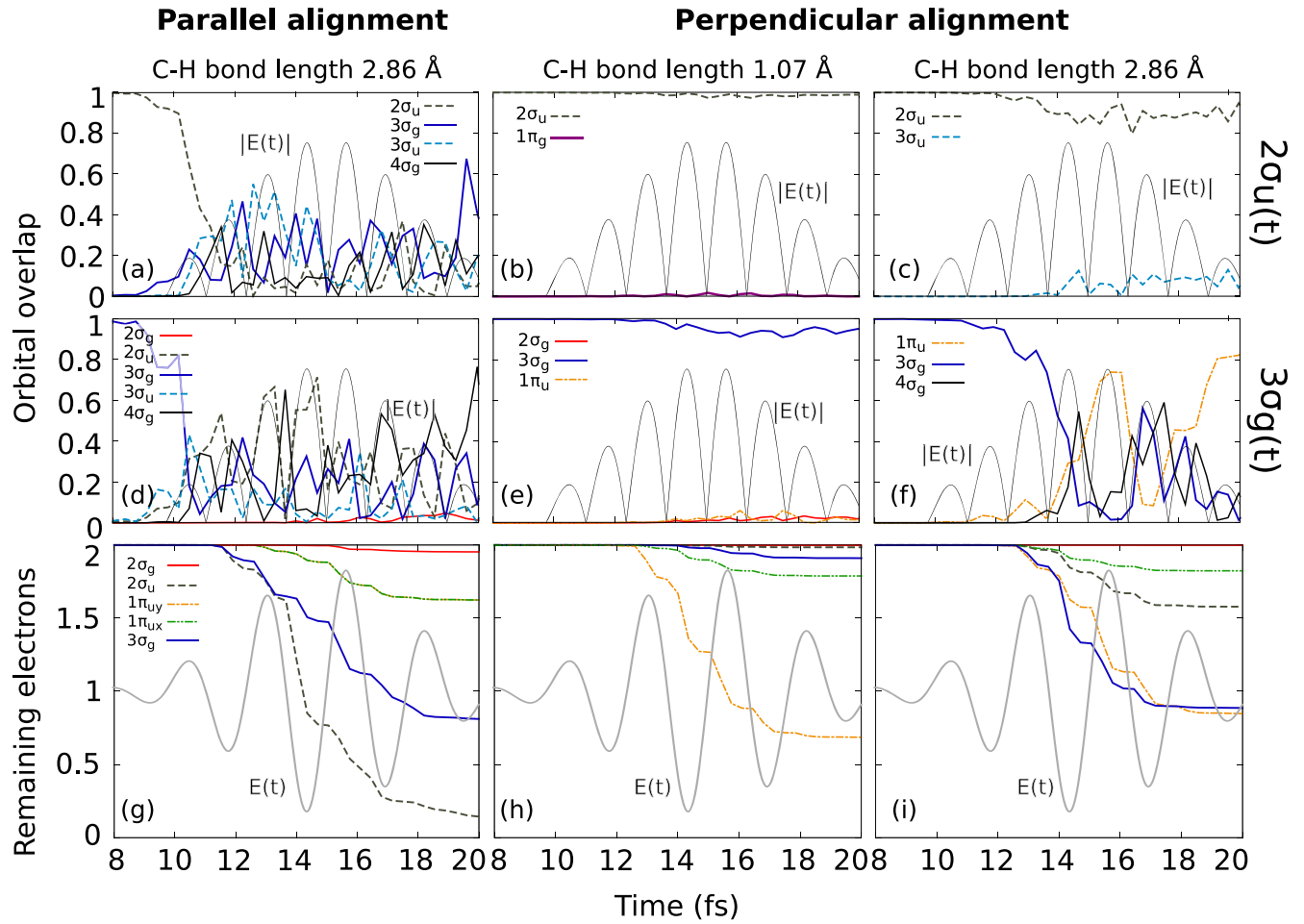


Figure 5. (a)–(f) TDDFT simulations of the evolution of overlap probabilities (as defined in the text) $P_{2\sigma_{u,j}}(t)$ (upper row) and $P_{3\sigma_{g,j}}(t)$ (middle row). Only the most relevant traces are shown. The ground state, time-independent orbitals j are indicated in each panel. The laser pulse parameters are as in figure 1. Parallel and perpendicular molecular alignment (the latter for two different C–H bond lengths), as indicated in the figure, are shown. (g)–(i) Evolution of the number of electrons $n_k(t)$ that remain bound in certain orbitals ψ_k (legend in panel (g)) during the laser pulse as defined by equation (5). The laser electric field $E(t)$ (normalised to an arbitrary peak value) is shown as a temporal reference in every panel.

identical to those used to compute the data for figure 1 and are given in section 2. We consider coupling of the two orbitals $3\sigma_g$ and $2\sigma_u$ to in total seven orbitals, $j = 1 \dots 7$. Four of the considered orbitals are the four most loosely bound, initially fully occupied orbitals $1\pi_u$, $3\sigma_g$, $2\sigma_u$, $2\sigma_g$ (in sequence of increasing binding energy), which constitute the HOMO, HOMO-1, HOMO-2 and HOMO-3 of acetylene. Note, that there exist actually two degenerate orbitals $1\pi_u$ ($1\pi_{u,x}$ and $1\pi_{u,y}$) which for parallel alignment remain degenerate and orthogonal to the σ -orbitals. For perpendicular alignment the symmetry gets broken and the two orbitals are no longer degenerate. Therefore, in figure 5 the traces of both of their overlap probabilities and of the ionisation yields from both of them are shown separately. To examine the involvement of higher lying orbitals in the ionisation behaviour we also consider coupling to the three most loosely bound initially unoccupied orbitals LUMO, LUMO+1, and LUMO+2, which for the equilibrium C–H internuclear distance are the orbitals $1\pi_g$, $4\sigma_g$ and $3\sigma_u$. For reasons of clarity we show in figure 5 only the most relevant traces $P_{3\sigma_{g,j}}(t)$ and $P_{2\sigma_{u,j}}(t)$ with a noticeable relative contribution. Note, that there also

exist two degenerate $1\pi_g$ orbitals, but one of them contributes negligibly. Although not essential for our analysis, we note in passing that because the energies of the orbitals increase differently with increasing C–H internuclear distance (figure 1), the ordering of the orbitals changes. For $R_{CH} = 2.86$ Å the LUMO, LUMO+1, and LUMO+2 are the $3\sigma_u$, $4\sigma_g$, and $1\pi_g$. The essential point is, though, that coupling to the loosely bound orbitals of the LUMO-complex is expected to constitute a particularly efficient ionisation mechanism, as subsequent field-ionisation from such weakly bound orbitals becomes strongly enhanced. In fact, for the equilibrium geometry, the LUMO+2 is already unbound. For $R_{CH} = 2.86$ Å the LUMO+2 is the last bound orbital. All higher lying ones are unbound.

Figure 5 shows that for parallel alignment the time-dependent $3\sigma_g$ and $2\sigma_u$ orbitals are strongly coupled with almost all other orbitals of σ -symmetry and become a superposition of the ground state orbitals $2\sigma_u$, $3\sigma_g$, $3\sigma_u$, and $4\sigma_g$. For comparison we show in figures 5(g)–(i) also the evolution of the number of electrons remaining in the five initially occupied orbitals, $n_k(t)$, calculated using equation (5).

In accordance with the experimental results and figure 1, for parallel alignment the by far largest share of electrons is emitted from the $2\sigma_u$ and $3\sigma_g$ orbitals. We concluded above that one reason for this is the strong geometrically induced upshift in energy at field-free conditions of these two orbitals for stretched C–H bonds with $R_{CH} \approx 2.5$ Å. From the quantities $P_{3\sigma_g j}(t)$ and $P_{2\sigma_u j}(t)$ in figure 5 we can now see that at $R_{CH} = 2.86$ Å these two states are additionally strongly coupled to the weakly bound LUMO complex, in particular to the $4\sigma_g$ orbital, from where ionisation can proceed very efficiently and which therefore leads to additional amplification of ionisation from the $3\sigma_g$ and $2\sigma_u$ orbitals.

This finding, that for stretched C–H bonds and parallel alignment the coupling to weakly bound σ -orbitals plays an essential role in the ionisation mechanism, provides additional explanation for the experimental observation that the proton yield angular distributions (figure 3) become strongly peaked along the molecular axis as soon as the regime of EI is reached: there are two effects at work. One is the narrowing of the ionisation rate along the molecular axis due to the repeated ionisation from σ -orbitals that we have described in section 4.1 above. The other effect that leads to narrow angular distributions is due to the strong coupling revealed by the TDDFT simulations.

This can be seen by the following simple considerations. The transition probabilities between the different orbitals i, j feature narrow cone-like angular distributions around the molecular axis determined by the projection of the transition dipole matrix elements $\vec{\mu}_{ij} = (\langle i|x|j\rangle, \langle i|y|j\rangle, \langle i|z|j\rangle)$ onto the laser polarisation axis. If we assume that the molecular axis is oriented along the z -direction and the transition takes place between σ orbitals then $\vec{\mu}_{ij} = (0, 0, \langle i|z|j\rangle)$ and we obtain $|\vec{E} \cdot \vec{\mu}|^2 = |\vec{E}| |\langle i|z|j\rangle| \cos(\theta)^2$ for the transition probability in a laser field \vec{E} whose polarisation direction is oriented by an angle θ to the molecular axis. For a multi-photon transition the angular dependence of the transition probability depends on the number of absorbed photons, n , as $|\vec{E} \cdot \vec{\mu}|^{2n}$, making its angular dependence even narrower. In the case considered here it is, however, difficult to quantify the number of absorbed photons. What we can infer from these considerations is that the angular dependence of the ionisation rate experiences an additional narrowing along the molecular axis due to the coupling between different orbitals, in perfect agreement with the experimental data. Thus, this finding from our simulations confirms our conclusions of a strongly enhanced contribution from lower-lying σ -orbitals to the ionisation yield that we have drawn above from the experimental results. In contrast, the corresponding TDDFT data for parallel aligned molecules with smaller (equilibrium) C–H distance $R_{CH} = 1.07$ Å (not depicted in figure 5), shows negligible coupling between the orbitals.

What are the reasons for the increased orbital mixing for parallel alignment at stretched C–H bonds? One reason is certainly that the orbital energies come closer with increasing R_{CH} (figure 1). Additionally, the transition dipole moments along the molecular (z -)axis increase for stretched C–H bonds as can be seen from the values given in table 1 for $R_{CH} = 1.07$

Table 1. Matrix elements along the molecular axis in units of eÅ.

	$R_{CH} = 1.07$ Å	$R_{CH} = 2.86$ Å
$\langle 2\sigma_u z 3\sigma_g \rangle$	1.14	1.51
$\langle 2\sigma_u z 4\sigma_g \rangle$	0.0715	−0.149
$\langle 3\sigma_g z 3\sigma_u \rangle$	−0.271	2.58

Å and $R_{CH} = 2.86$ Å. All of the transition dipole moments increase with R_{CH} , but in particular the couplings to the very weakly bound orbitals in the LUMO complex increase very strongly. For example, for transitions between the $3\sigma_g$ and $3\sigma_u$ orbitals the magnitude of the transition dipole moment increases by roughly one order of magnitude, i.e., transitions become more likely by roughly a factor of 100. Thus, we identify the combined consequences of a geometrically induced field-free energy upshift of the bound orbitals and the strongly increased coupling to higher-lying orbitals as the main ingredients of EIC-MOUSE, which we have herewith identified as the driving mechanism behind the EI at stretched C–H distances that we observe experimentally for molecules aligned parallel to the laser polarisation direction, see section 3.

Coupling between orbitals of different symmetry (e.g. σ_u and σ_g) may lead to oscillatory charge-localisation at different sides of the molecule. Such oscillatory localisation of charge at the energy-upshifted potential well is one of the main ingredients in the CREI mechanism [3, 4, 17]. In the EIC-MOUSE mechanism not only two but several orbitals of different symmetry are coupled by the laser field. In that case, a more complicated or even random evolution of the localisation is expected. Indeed, the TDDFT simulations predict a complicated sub-cycle charge-localisation pattern for molecules with stretched bonds aligned parallel to the laser polarisation direction, see figure 6. The charge density, both the integrated one and that in specific orbitals, overall features oscillations at the laser frequency. But the positions do not adiabatically follow the laser field oscillations nor does the charge localise periodically on either end of the molecule. The charge density corresponding to the $2\sigma_u$ orbital even stays on the negative side for more than one laser oscillation cycle. To some extent this asymmetry is probably due to the contributions of the ionising electron cloud while it is departing along the laser field direction. Still, taking this into account, we infer from figure 6 that periodic charge-localisation as in the CREI mechanism is not a pre-requisite for the efficient emission of several electrons during the pulse (the evolution of the electron loss is shown for comparison in figure 6). This is one of the features that renders the EIC-MOUSE mechanism described here different from CREI. More distincting features are described in section 5.

Let us now turn to the case when the molecules are aligned perpendicularly to the laser polarisation direction. The centre column of figure 5 shows that at the equilibrium C–H inter-nuclear distance of $R_{CH} = 1.07$ Å the coupling of the HOMO-1 and HOMO-2 orbitals ($3\sigma_g$ and $2\sigma_u$) with other orbitals is very weak and the dominant contribution to the ionisation yield comes from the HOMO $1\pi_u$ (figure 5(h)). The right column of figure 5, depicting data for a stretched C–H distance of

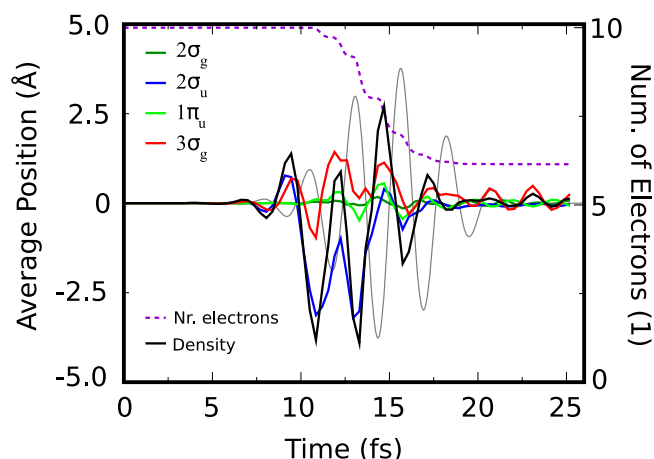


Figure 6. Average position of the charge density, overall and in selected orbitals, as indicated by different colours in the figure, simulated by TDDFT for a pulse with the same parameters as in figure 1. The molecular alignment was assumed parallel to the laser polarisation direction and the internuclear distance was 2.86 Å for both C–H bonds. The laser electric field normalised to an arbitrary value (grey line) is shown for temporal reference. Additionally the evolution of the total number of electrons remaining in the molecule is shown. See caption of figure 5 for technical details on this quantity.

$R_{\text{CH}} = 2.86$ Å, shows that for stretched bonds also for the perpendicular alignment certain orbitals would couple significantly—in particular the time-dependent $3\sigma_g$ orbital mixes strongly with the $1\pi_u$ orbital—which would lead to significant emission of electrons from both the $1\pi_u$ and $3\sigma_g$ orbitals (see figure 5(i)). However, during the initial ionisation step(s) of perpendicularly aligned acetylene molecules at their equilibrium C–H distance, almost exclusively π electrons are ejected (figure 5(h)). The important point is that ejection of π electrons does not affect the C–H bond which is formed by the σ orbitals only. Therefore, ionisation of perpendicularly aligned molecules does not entail stretching of the C–H internuclear distance. The TDDFT data depicted in the right column, calculated for molecules with a C–H distance fixed at $R_{\text{CH}} = 2.86$ Å, is therefore a very unlikely situation that only takes place for the small percentage of molecules for which initially σ electrons are ejected. The same is true for the data in figure 1(d) for stretched C–H bonds. As a consequence of the fact that stretching of the C–H bonds is largely inhibited for perpendicular alignment, the two mechanisms leading to EI for the parallel molecular alignment that we described above are inhibited for perpendicular alignment. In turn, molecules aligned perpendicularly to the laser polarisation direction enter the regime of EI at stretched C–H bonds only with a very small probability. Thus, the chance of observing high charge states $z \geq +4$ for perpendicularly aligned molecules is negligible, which is exactly what our measurements show, see section 3.

5. Conclusions

In conclusion, we investigated the intensely debated mechanism behind the process of efficient laser-ionisation of polyatomic molecules that results in the emission of multiple

electrons during the interaction with ultrashort intense laser pulses. By a combined experimental and numerical approach based on coincidence momentum spectroscopy and TDDFT simulations and using the acetylene molecule as a model system we succeeded in establishing an intuitive explanation for the surprisingly high charge states measured in experiments conducted with quite moderate laser peak intensities [18, 29–33].

Analysis of measured proton angular yield distributions for a range of laser pulse durations and peak intensities allowed us to identify a clear transition to a regime where the ionisation from lower lying orbitals becomes strongly enhanced at stretched internuclear C–H distances for molecules aligned parallel to the laser polarisation direction. No enhancement is observed for perpendicular molecular alignment. In contrast to the well-known CREI mechanism [3, 4, 17] the current EI mechanism for parallel molecular alignment is observed for a plateau of C–H distances rather than only a critical internuclear distance, in agreement with recent theoretical predictions [34].

By the complementary insight obtained through the TDDFT simulations we could show that the strong ionisation enhancement for molecules aligned parallel to the laser polarisation direction is due to the combination of a strong increase in the coupling between σ orbitals (also to weakly bound and even unbound orbitals from the LUMO complex) and the geometrically induced energy upshift of the orbitals as the C–H internuclear distance increases beyond a certain value (about 2.5 Å for acetylene, roughly 2–2.5 times the internuclear distance). The reason for the increased coupling is the increase of the dipole transition matrix elements and the closeness of the energy levels. For molecules aligned perpendicularly to the laser polarisation direction this mechanism is inhibited, since at the equilibrium C–H internuclear distance dominantly π electrons are ejected which does not result in a stretch of the C–H bonds that is necessary for entering the regime of EI.

The EIC-MOUSE mechanism described here shows a number of features that render it different from the CREI mechanism [3, 4, 17] that has been found as the underlying mechanism in most previous works on molecular ionisation [5, 9, 14, 15, 20–27]. The first important feature of EIC-MOUSE is that it builds on the strong energy upshift at field-free conditions of multiple orbitals for stretched molecular configuration which, secondly, leads to EI for molecules stretched *beyond* a certain critical internuclear distance rather than only *around* the critical internuclear distance. In the EI regime, thirdly, the laser-field-induced coupling between *multiple* orbitals becomes crucial, whereas for CREI only *two* charge-resonant states are coupled. Fourth, in EIC-MOUSE not only the coupling between bound orbitals but also coupling with high-lying and potentially unbound orbitals contributes to the EI. Although certainly not the last distinction we stop this incomplete enumeration by acknowledging, fifth, the differences between CREI and EIC-MOUSE concerning the charge localisation: while for CREI the laser-driven coupling of the two (charge-resonant) orbitals results in an oscillatory charge-localisation at two different locations inside the molecule, which is a necessary condition for efficient ionisation from the energy-upshifted potential well at the critical internuclear distance, the

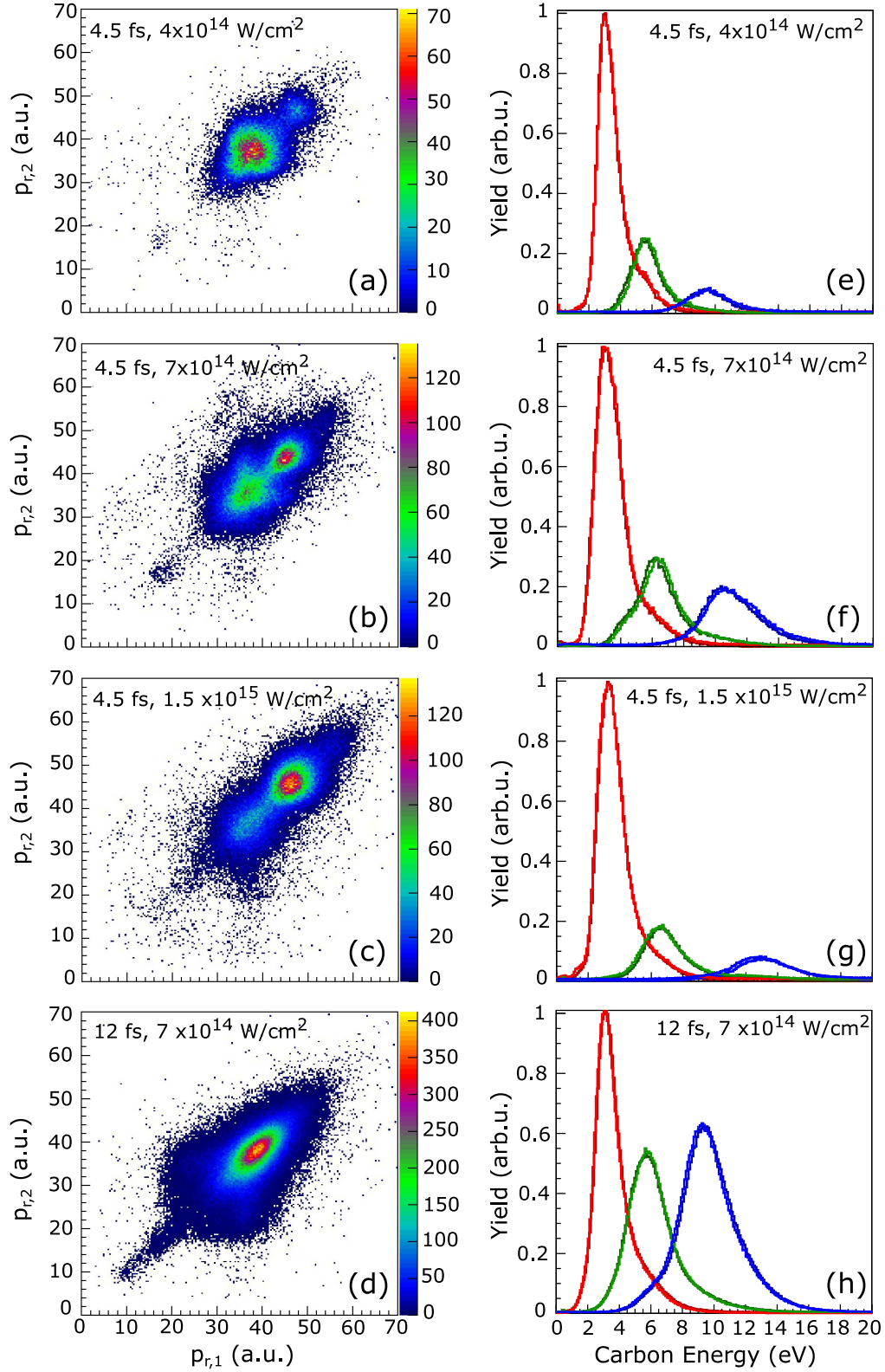


Figure A1. (left column) Coincidence momentum distributions for the two protons ejected during fragmentation of acetylene into $C^+/C^+/H^+/H^+$. Depicted is the momentum magnitude of one proton $p_r = \sqrt{p_x^2 + p_y^2 + p_z^2}$ (with $|p_x| < 10$ au) versus that of the other proton for different laser pulse parameters as indicated in the panels. (right column) Carbon energy distributions for different laser pulse durations and peak intensities (indicated in the panels) for three different four-body fragmentation channels $C^{m+}/C^{n+}/H^+/H^+$: $m = n = 1$ (red line); $m = 2, n = 1$ (green line); $m = 2, n = 2$ (blue line). The distributions for both carbons are shown on top of each other with lines of slightly different brightness.

coupling of the multiple orbitals in EIC-MOUSE does, in contrast, not necessarily lead to oscillatory charge localisation, and is also not required (see figure 6).

We think that the EIC-MOUSE mechanism, described here for the example of acetylene, can also explain the high charge states measured in many experiments on various hydrocarbon molecules, e.g., [18, 29–33]. Furthermore, the fact that the effects of a close energy spacing, strong contributions from lower-valence orbitals and an enhancement of the ionisation for an internuclear distance stretched beyond a certain value (rather than a peak of the ionisation at a critical internuclear distance) have also been identified in the ionisation of CO₂ [25], suggests that EIC-MOUSE, contrary to the previously given explanation, is also at work for this molecule. This therefore indicates that EIC-MOUSE is a general mechanism that is not restricted to hydrocarbons.

Acknowledgments

We acknowledge financial support by the Austrian Science Fund (FWF) under grants P28475-N27, P21463-N22, P25615-N27, P27491-N27, SFB-F49 NEXTLite, by a starting grant from the ERC (project CyFi), by the National Science Foundation (NSF) under grants Phy 1314463 and IIA126117, and by the Japan Society for the Promotion of Science (JSPS KAKENHI) under grants 15K17805, 24245003, and 15H05696.

Appendix. Proton coincidence distributions: concerted proton ejection

In deriving the proton angular yield distributions of figure 3 we made use of the fact that the two protons are ejected simultaneously (concertedly) and in a back-to-back manner. Here we confirm this dynamic using a combination of two-proton coincidence and carbon energy distributions.

The right column of figure A1 shows carbon energy distributions for different laser pulse durations and peak intensities resulting from a four-body coincidence selection as indicated in the figure caption. It can be seen that all of them exhibit a smooth shape and only consist of a single peak for each charge state, even when the proton distributions (left column) are bimodal. We infer from this that the explosion of the carbon skeleton structure happens in a back-to-back manner with the two carbon ions fulfilling momentum conservation, uninfluenced by the proton ejection process. This means that the explosion of the carbon skeleton structure must happen long after the protons have been ejected.

The first step of the explosion of the molecular ions is therefore the emission of the two protons. The left column of figure A1 shows two-proton coincidence momentum distributions for the momentum magnitudes p_r . The two-proton momentum distributions are closely aligned along the diagonal, which shows that the two protons are emitted back-to-back, i.e., with the same momentum magnitude but into opposite directions. On a closer look there can be two peaks noticed in the

coincidence momentum distributions for short pulse duration (figures A1(a)–(c)). This interesting, thus far not observed feature is discussed in detail in section 3. It is important to note, however, that *all* peaks of the proton coincidence momentum distributions are situated along the diagonal, i.e., are generated by back-to-back proton emission. The fact that the two protons exhibit the same momentum magnitude but are ejected into opposite directions justifies our procedure for obtaining the 3D momentum distributions of figure 2. For these we plotted the momentum distribution of that proton that arrives at the detector earlier and then symmetrized the distributions about p_y .

ORCID

Markus Koch  <https://orcid.org/0000-0003-0186-1614>

References

- [1] Krausz F and Ivanov M 2009 Attosecond physics *Rev. Mod. Phys.* **81** 163–234
- [2] Ivanov M Y, Spanner M and Smirnova O 2005 Anatomy of strong field ionization *J. Mod. Opt.* **52** 165–84
- [3] Seideman T, Ivanov M and Corkum P 1995 Role of electron localization in intense-field molecular ionization *Phys. Rev. Lett.* **75** 2819–22
- [4] Zuo T and Bandrauk A D 1995 Charge-resonance-enhanced ionization of diatomic molecular ions by intense lasers *Phys. Rev. A* **52** R2511–4
- [5] Bandrauk A D and Ruel J 1999 Charge-resonance-enhanced ionization of molecular ions in intense laser pulses: geometric and orientation effects *Phys. Rev. A* **59** 2153–62
- [6] Pavičić D, Kiess A, Hänsch T W and Figger H 2005 Intense-laser-field ionization of the hydrogen molecular ions H₂⁺ and D₂⁺ at critical internuclear distances *Phys. Rev. Lett.* **94** 163002
- [7] Kjeldsen T K, Madsen L B and Hansen J P 2006 *Ab initio* studies of strong-field ionization of arbitrarily oriented H₂⁺ molecules *Phys. Rev. A* **74** 035402
- [8] Lagmago Kamta G and Bandrauk A 2007 Effects of molecular symmetry on enhanced ionization by intense laser pulses *Phys. Rev. A* **75** 041401
- [9] Suzuki N, Kawata I and Yamashita K 2007 Comparison of the mechanisms of enhanced ionization of H₂ and H₃⁺ in intense laser fields *Chem. Phys.* **338** 348–53
- [10] Takemoto N and Becker A 2010 Multiple ionization bursts in laser-driven hydrogen molecular ion *Phys. Rev. Lett.* **105** 203004
- [11] Takemoto N and Becker A 2011 Time-resolved view on charge-resonance-enhanced ionization *Phys. Rev. A* **84** 023401
- [12] Strickland D, Beaudoin Y, Dietrich P and Corkum P 1992 Optical studies of inertially confined molecular iodine ions *Phys. Rev. Lett.* **68** 2755–8
- [13] Constant E, Stapelfeldt H and Corkum P B 1996 Observation of enhanced ionization of molecular ions in intense laser fields *Phys. Rev. Lett.* **76** 4140–3
- [14] Chen H, Fang L, Tagliamonti V and Gibson G N 2011 Angle-resolved and internuclear-separation-resolved measurements of the ionization rate of the B state of I₂ by strong laser fields *Phys. Rev. A* **84** 043427
- [15] Chen H, Tagliamonti V and Gibson G N 2012 Enhanced ionization of an inner orbital of I₂ by strong laser fields *Phys. Rev. A* **86** 051403

- [16] Frasinski L, Codling K, Hatherly P, Barr J, Ross I and Toner W 1987 Femtosecond dynamics of multielectron dissociative ionization by use of a picosecond laser *Phys. Rev. Lett.* **58** 2424–7
- [17] Codling K, Frasinski L J and Hatherly P A 1989 On the field ionisation of diatomic molecules by intense laser fields *J. Phys. B: At. Mol. Opt. Phys.* **2** L321–7
- [18] Cornaggia C, Normand D and Morellec J 1992 Role of the molecular electronic configuration in the Coulomb fragmentation of N_2 , C_2H_2 and C_2H_4 in an intense laser field *J. Phys. B: At. Mol. Opt. Phys.* **5** L415–22
- [19] Schmidt M, Normand D and Cornaggia C 1994 Laser-induced trapping of chlorine molecules with pico- and femtosecond pulses *Phys. Rev. A* **50** 5037–45
- [20] Dehghanian E, Bandrauk A D and Lagmago Kamta G 2013 Enhanced ionization of the non-symmetric HeH^+ molecule driven by intense ultrashort laser pulses *J. Chem. Phys.* **139** 084315
- [21] Lagmago Kamta G and Bandrauk A D 2007 Nonsymmetric molecules driven by intense few-cycle laser pulses: phase and orientation dependence of enhanced ionization *Phys. Rev. A* **76** 053409
- [22] Hishikawa A, Iwamae A and Yamanouchi K 1999 Ultrafast structural deformation of NO_2 in intense laser fields studied by mass-resolved momentum imaging *J. Chem. Phys.* **111** 8871
- [23] Ueyama M, Hasegawa H, Hishikawa A and Yamanouchi K 2005 Concerted and sequential Coulomb explosion processes of N_2O in intense laser fields by coincidence momentum imaging *J. Chem. Phys.* **123** 154305
- [24] Hishikawa A, Iwamae A and Yamanouchi K 1999 Ultrafast deformation of the geometrical structure of CO_2 induced in intense laser fields *Phys. Rev. Lett.* **83** 1127–30
- [25] Bocharova I *et al* 2011 Charge resonance enhanced ionization of CO_2 probed by laser Coulomb explosion imaging *Phys. Rev. Lett.* **107** 063201
- [26] Wu J, Meckel M, Schmidt L P H, Kunitski M, Voss S, Sann H, Kim H, Jahnke T, Czasch A and Dörner R 2012 Probing the tunnelling site of electrons in strong field enhanced ionization of molecules *Nat. Commun.* **3** 1113
- [27] Wu J, Gong X, Kunitski M, Amankona-Diawuo F K, Schmidt L P H, Jahnke T, Czasch A, Seideman T and Dörner R 2013 Strong field multiple ionization as a route to electron dynamics in a van der Waals cluster *Phys. Rev. Lett.* **111** 083003
- [28] Siedschlag C and Rost J-M 2003 Enhanced ionization in small rare gas-clusters *Phys. Rev. A* **67** 013404
- [29] Roither S *et al* 2011 High energy proton ejection from hydrocarbon molecules driven by highly efficient field ionization *Phys. Rev. Lett.* **106** 163001
- [30] Bubin S, Atkinson M, Varga K, Xie X, Roither S, Kartashov D, Baltuška A and Kitzler M 2012 Strong laser-pulse-driven ionization and Coulomb explosion of hydrocarbon molecules *Phys. Rev. A* **86** 043407
- [31] Xie X *et al* 2014 Role of proton dynamics in efficient photoionization of hydrocarbon molecules *Phys. Rev. A* **89** 023429
- [32] Cornaggia C 2016 Electronic dynamics of charge resonance enhanced ionization probed by laser-induced alignment in C_2H_2 *J. Phys. B: At. Mol. Opt. Phys.* **49** 19LT01
- [33] Cornaggia C, Schmidt M and Normand D 1995 Laser-induced nuclear motions in the Coulomb explosion of $C_2H_2^+$ ions *Phys. Rev. A* **51** 1431–7
- [34] Lötstedt E, Kato T and Yamanouchi K 2013 Intramolecular electron dynamics in the ionization of acetylene by an intense laser pulse *J. Chem. Phys.* **138** 104304
- [35] Russakoff A, Bubin S, Xie X, Erattupuzha S, Kitzler M and Varga K 2015 Time-dependent density-functional study of the alignment-dependent ionization of acetylene and ethylene by strong laser pulses *Phys. Rev. A* **91** 023422
- [36] Lötstedt E, Kato T and Yamanouchi K 2012 Enhanced ionization of acetylene in intense laser fields *Phys. Rev. A* **85** 041402
- [37] Lötstedt E, Kato T and Yamanouchi K 2012 Efficient ionization of one-dimensional acetylene investigated by time-dependent Hartree–Fock calculations *Phys. Rev. A* **86** 023401
- [38] Xie X, Lötstedt E, Roither S, Schöffler M, Kartashov D, Midorikawa K, Baltuška A, Yamanouchi K and Kitzler M 2015 Duration of an intense laser pulse can determine the breakage of multiple chemical bonds *Sci. Rep.* **5** 12877
- [39] Xie X *et al* 2014 Selective control over fragmentation reactions in polyatomic molecules using impulsive laser alignment *Phys. Rev. Lett.* **112** 163003
- [40] Xie X *et al* 2014 Electronic predetermination of ethylene fragmentation dynamics *Phys. Rev. X* **4** 021005
- [41] Doblhoff-Dier K 2014 Strong-field dynamics in small molecules *PhD Thesis* Technische Universität Wien
- [42] Doblhoff-Dier K, Kitzler M and Gräfe S 2016 Theoretical investigation of alignment-dependent intense-field fragmentation of acetylene *Phys. Rev. A* **94** 013405
- [43] Troullier N and Martins J L 1991 Efficient pseudopotentials for plane-wave calculations *Phys. Rev. B* **43** 1993–2006
- [44] Perdew J P and Zunger A 1981 Self-interaction correction to density-functional approximations for many-electron systems *Phys. Rev. B* **23** 5048–79
- [45] de Morisson Faria C F and Liu X 2011 Electron–electron correlation in strong laser fields *J. Mod. Opt.* **58** 1076–131
- [46] Schöffler M S, Xie X, Wustelt P, Möller M, Roither S, Kartashov D, Sayler A M, Baltuska A, Paulus G G and Kitzler M 2016 Laser-subcycle control of sequential double-ionization dynamics of helium *Phys. Rev. A* **93** 063421
- [47] Son S-K and Chu S-I 2009 Multielectron effects on the orientation dependence and photoelectron angular distribution of multiphoton ionization of CO_2 in strong laser fields *Phys. Rev. A* **80** 011403
- [48] De Giovannini U, Varsano D, Marques M A L, Appel H, Gross E K U and Rubio A 2012 *Ab initio* angle- and energy-resolved photoelectron spectroscopy with time-dependent density-functional theory *Phys. Rev. A* **85** 062515
- [49] Tong X M, Zhao Z X, Alnaser A S, Voss S, Cocke C L and Lin C D 2005 Post ionization alignment of the fragmentation of molecules in an ultrashort intense laser field *J. Phys. B: At. Mol. Opt. Phys.* **38** 333–41
- [50] Dörner R, Mergel V, Jagutzki O, Spielberger L, Ullrich J, Moshhammer R and Schmidt-Böcking H 2000 Cold target recoil ion momentum spectroscopy: a ‘momentum microscope’ to view atomic collision dynamics *Phys. Rep.* **330** 95–192
- [51] Zhang L *et al* 2012 Path-selective investigation of intense laser-pulse-induced fragmentation dynamics in triply charged 1,3-butadiene *J. Phys. B: At. Mol. Opt. Phys.* **45** 085603
- [52] Sayler A M, Rathje T, Müller W, Kürbis C, Rühle K, Stibenz G and Paulus G G 2011 Real-time pulse length measurement of few-cycle laser pulses using above-threshold ionization *Opt. Express* **19** 4464
- [53] Sayler A M, Rathje T, Müller W, Rühle K, Kienberger R and Paulus G G 2011 Precise, real-time, every-single-shot, carrier-envelope phase measurement of ultrashort laser pulses *Opt. Lett.* **36** 1
- [54] Alnaser A, Tong X, Osipov T, Voss S, Maharjan C, Shan B, Chang Z and Cocke C 2004 Laser-peak-intensity calibration using recoil-ion momentum imaging *Phys. Rev. A* **70** 23413
- [55] Smeenk C, Salvail J Z, Arissian L, Corkum P B, Hebeisen C T and Staudte A 2011 Precise *in situ* measurement of laser pulse intensity using strong field ionization *Opt. Express* **19** 9336
- [56] Linstrom P and Mallard W NIST Chemistry WebBook, NIST Standard Reference Database Number 69 (<http://webbook.nist.gov>)